BIOCHEMISTRY
including biophysical chemistry & molecular biology

Article

pubs.acs.org/biochemistry

The Structure of an Oxalate Oxidoreductase Provides Insight into Microbial 2-Oxoacid Metabolism

Marcus I. Gibson,[†] Edward J. Brignole,[†,‡] Elizabeth Pierce,[§,⊥] Mehmet Can,[§] Stephen W. Ragsdale,[§] and Catherine L. Drennan*[,†,‡,∥]

[†]Department of Chemistry, Massachusetts Institute of Technology, 77 Massachusetts Avenue, Cambridge, Massachusetts 02139, United States

[‡]Howard Hughes Medical Institute, Massachusetts Institute of Technology, 77 Massachusetts Avenue, Cambridge, Massachusetts 02139, United States

[§]Department of Biological Chemistry, University of Michigan, Ann Arbor, Michigan 48109, United States

[∥]Department of Biology, Massachusetts Institute of Technology, 77 Massachusetts Avenue, Cambridge, Massachusetts 02139, United States

Supporting Information

ABSTRACT: Thiamine pyrophosphate (TPP), a derivative of vitamin B_1, is a versatile and ubiquitous cofactor. When coupled with [4Fe-4S] clusters in microbial 2-oxoacid:ferredoxin oxidoreductases (OFORs), TPP is involved in catalyzing low-potential redox reactions that are important for the synthesis of key metabolites and the reduction of N_2, H^+, and CO_2. We have determined the high-resolution (2.27 Å) crystal structure of the TPP-dependent oxalate oxidoreductase (OOR), an enzyme that allows microbes to grow on oxalate, a widely occurring dicarboxylic acid that is found in soil and freshwater and is responsible for kidney stone disease in humans. OOR catalyzes the anaerobic oxidation of oxalate, harvesting the low-potential electrons for use in anaerobic reduction and fixation of CO_2. We compare the OOR structure to that of the only other structurally characterized OFOR family member, pyruvate:ferredoxin oxidoreductase. This side-by-side structural analysis highlights the key similarities and differences that are relevant for the chemistry of this entire class of TPP-utilizing enzymes.

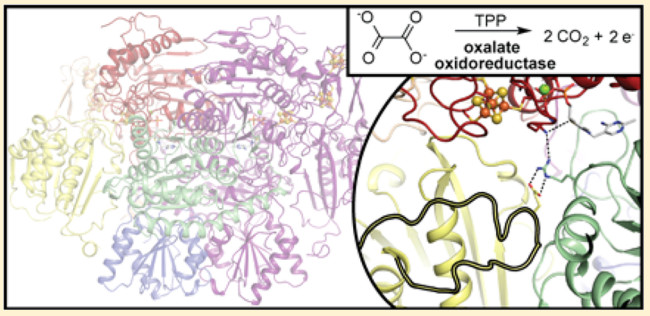

2-Oxoacid:ferredoxin oxidoreductases (OFORs) make up an ancient family of enzymes that use thiamine pyrophosphate (TPP) and three [4Fe-4S] clusters to perform essential carbon fixation and redox reactions in microbes. Key to OFOR chemistry is the ability of the TPP cofactor to act as a potent nucleophile and form covalent adducts with the 2-oxoacid substrates, reversibly cleaving a carbon−carbon bond and generating electrons capable of reducing low-potential ferredoxins. This enzyme family predates the divergence of archaea and eukaryotes, and members are ubiquitous in archaea, common in bacteria, and present in a handful of anaerobic eukaryotes.[1,2] The most well-studied members of this family are the pyruvate:ferredoxin oxidoreductases (PFORs), which interconvert pyruvate with acetyl-coenzyme A (acetyl-CoA) and carbon dioxide (Scheme 1a). The formation of pyruvate from acetyl-CoA and CO_2 by PFOR is required in all modes of anaerobic CO_2 fixation,[3] allowing for assimilation of acetyl-CoA into other central metabolites by a number of different routes: the reductive citric acid cycle in photosynthetic bacteria,[4,5] the Wood−Ljungdahl (W−L) pathway in aceto-genic and sulfate-reducing bacteria as well as in methanogenic archaea (Figure 1),[6] and bicycles in several classes of archaea.[3] In the opposite direction, the oxidation of pyruvate by PFOR releases two low-potential electrons (E_0' = −515 mV,[7,8] at pH 7.0) that can be used by acetogens to reduce CO_2 in the W−L pathway and by many organisms to reduce dinitrogen to ammonia or protons to hydrogen gas.[9−11] Similarly, the reducing equivalents harvested from α-ketoglutarate oxidation

Scheme 1. Redox Reactions Catalyzed by (a) PFOR and (b) OOR

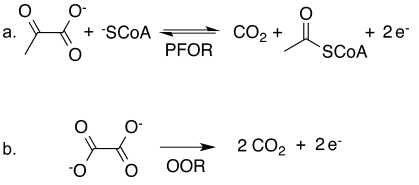

Received: May 13, 2015
Revised: June 10, 2015
Published: June 10, 2015

DOI: 10.1021/acs.biochem.5b00521
Biochemistry 2015, 54, 4112−4120

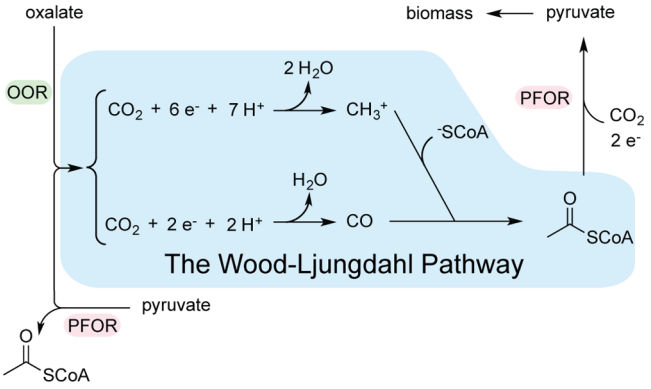

Figure 1. Overall transformation performed by the Wood–Ljungdahl pathway in *Moorella thermoacetica* and connection to OOR and PFOR. PFOR can operate on both ends of the W–L pathway. PFOR can cleave pyruvate to generate both CO_2 and reducing equivalents for the W–L pathway, and it can produce pyruvate as a means of assimilating the acetyl-CoA produced by the W–L pathway. In the presence of oxalate, *M. thermoacetica* uses OOR to generate CO_2 and reducing equivalents for the production of acetyl-CoA via the W–L pathway.

by 2-oxoglutarate:ferredoxin oxidoreductase can be used by organisms such as *Thauera aromatica* to reduce and metabolize aromatic compounds.[12] The low potential of the electrons released by 2-oxoacid oxidation by OFORs has also allowed for antimicrobial targeting by drugs such as metronidazoles, which require reductive activation in the potential range of −500 to −260 mV.[13]

Despite the ubiquity of this family of enzymes in microbial life and the volume of work that has been done to understand function, genetics, and evolution, to date only one OFOR has been structurally characterized to atomic resolution, the PFOR from *Desulfovibrio africanus* (*Da* PFOR).[14−16] A series of structures of *Da* PFOR revealed the active site architecture around the TPP cofactor and allowed for the visualization of the arrangement of the three [4Fe-4S] clusters that serve to transport electrons from the active site to the protein surface, where they can be transferred to other redox partners. However, broader applicability of this enzyme's structure to other OFOR family members is limited by a handful of peculiar features. Most notably, *Da* PFOR's domain VII, which is a 60-residue C-terminal peptide region that interacts directly with the active site and with the ferredoxin domain, is not found in any other PFORs or in any OFOR so far identified. Thus, the one available view of the active site is unlikely to be representative. Additionally, *Da* PFOR is part of a subgroup of PFORs that are homodimers of single-chain fusions of the functional domains, whereas other PFORs are composed of up to four different protein chains in the catalytic unit,[1] suggesting that other differences may be found among this family of enzymes with respect to subunit–subunit arrangements.

Here we present the second structure of an enzyme in this superfamily, and the first crystal structure of an oxalate oxidoreductase (OOR). This enzyme from *Moorella thermoacetica* uses TPP to oxidize oxalate to two molecules of CO_2, generating two low-potential electrons, which can be transferred to other electron acceptors via three enzyme-bound [4Fe-4S] clusters (Scheme 1b). OOR is a member of the OFOR family of enzymes that is unique in that it does not require CoA, a nucleotide-based organic thiol, for catalysis. It also represents a previously unknown anaerobic pathway for oxalate metabolism.[17−19] Before the discovery of OOR, known oxalate-metabolizing enzymes fell into one of three metabolic pathways (see Figure S1 of the Supporting Information). The first of these pathways is characterized by oxalate oxidases, which produce two molecules of CO_2 while reducing molecular oxygen to H_2O_2, a product that has a role in signaling and defense in plants.[20−22] The second pathway makes use of oxalate decarboxylases, found mostly in fungi and some bacteria. Oxalate decarboxylases require molecular oxygen for activity but perform instead a disproportionation reaction, generating CO_2 and formate from oxalate.[23] These first two pathways share a requirement for a manganese cofactor and molecular oxygen for activity but do not require CoA. The third pathway, the only pathway previously established to anaerobically metabolize oxalate, involves oxalyl-CoA decarboxylase, which is a TPP-dependent enzyme.[24] Oxalyl-CoA decarboxylases, like their Mn-dependent counterparts, produce CO_2 and formate (in the form of formyl-CoA), the latter of which can be used either to generate NADH[25] or, as in *Oxalobacter formigenes*, to create a membrane potential for the production of ATP.[26] As implied in the name, however, oxalyl-CoA decarboxylases require CoA for activity. In comparison, OOR is a hybrid of these other oxalate-metabolizing enzymes. It is similar to the aerobic family members in the lack of a requirement for CoA; however, the cofactor usage is different (TPP instead of Mn^{2+}) and the oxygen dependence different, whereas OOR and the other anaerobic oxalate-metabolizing enzyme share the same dependence in their use of one cofactor (TPP) but differ in their use of the other, CoA.

The role of oxalate in biological systems is multifaceted. As mentioned above, microbes and plants use electrons generated by its cleavage in processes ranging from energy generation to signaling. Humans do not metabolize oxalate, and accumulation is associated with kidney stone formation.[27] In the model acetogen *M. thermoacetica*, the role of oxalate is particularly complex. At a regulatory level, growth on oxalate upregulates the W–L pathway, even under conditions in which the W–L pathway is generally suppressed.[28] At a molecular level, cleavage of oxalate by OOR can provide both the low-potential electrons and the CO_2 substrate for carbon monoxide dehydrogenase/acetyl-CoA synthase, the key enzyme in this pathway,[19] allowing *M. thermoacetica* to grow exclusively on oxalate.[17] Here our structure of *M. thermoactica* OOR provides new insight into this unique pathway for oxalate metabolism, as well as into the larger superfamily of OFORs.

MATERIALS AND METHODS

Protein Purification. OOR was purified from its native organism, *M. thermoacetica*, by the methods described previously,[19] concentrated to 45 mg/mL, as determined by the rose bengal method[29] with a lysozyme standard, and stored in a storage buffer [50 mM Tris (pH 8.0) and 2 mM dithiothreitol] at room temperature under an anoxic nitrogen atmosphere.

Crystallization. OOR was crystallized by the hanging drop method at room temperature in a Coy anaerobic chamber under an Ar/H_2 gas mixture. OOR (30 mg/mL) in the storage buffer was mixed with the well solution [8–11% PEG 3000 and 3–4% Tacsimate (pH 7.0)] in a 1:1 ratio to make a 2 μL hanging drop with a final protein concentration of 15 mg/mL. Crystals large enough for data collection grew in 2–4 days without any additional crystallization aids. Long, rodlike crystals grew in orthorhombic space group $P2_12_12_1$, but with varying cell constants. The crystal used for collecting multiwavelength

DOI: 10.1021/acs.biochem.5b00521
Biochemistry 2015, 54, 4112–4120

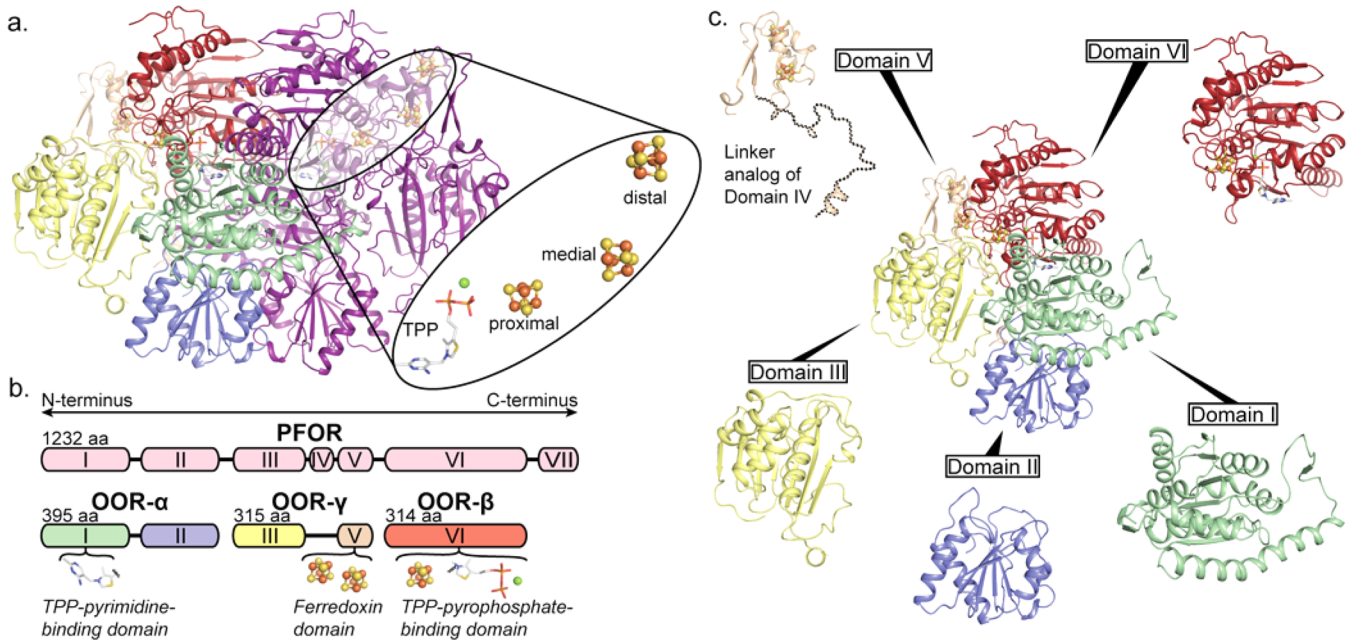

Figure 2. Structure and domain arrangement of OOR. (a) Ribbon drawing of the OOR dimer. The right $\alpha\gamma\beta$ monomeric unit is colored purple, and the left monomeric unit is colored by domain. The insert highlights the spatial arrangement of the TPP and [4Fe-4S] cofactors of the right monomeric unit, with Mg^{2+} as a green sphere. (b) Cartoon of the domain arrangement for the catalytic units of *Da* PFOR on top and OOR ($\alpha\gamma\beta$) on the bottom. Domains are indicated with colored boxes, with their respective domain numbers inside. Black bars connecting domains indicate that the domains are found on the same polypeptide chain. Ligand binding function is indicated below the domains of OOR. OOR-α forms domains I (residues 1−250) and II (residues 251−395); OOR-γ comprises domains III (residues 1−217) and V (residues 238−315), and OOR-β comprises domain VI (residues 1−314). Domain I binds the pyrimidine moiety of TPP; domain V binds the medial and distal [4Fe-4S] clusters, and domain VI binds the proximal [4Fe-4S] cluster as well as the pyrophosphate moiety of TPP. Domains IV and VII are only present in *Da* PFOR. (c) The domains of OOR are shown both individually and in the context of the OOR catalytic $\alpha\gamma\beta$ unit.

anomalous dispersion (MAD) data had the following unit cell constants: a = 114 Å, b = 145 Å, and c = 163 Å; the crystal used for collecting native data had the following unit cell constants: a = 84 Å, b = 152 Å, and c = 172 Å.

Before being cryocooled, the crystals for MAD and native data were first cryoprotected using a solution of 15% PEG 3000, 2% Tacsimate (pH 7.0), 20% PEG 400, and 50% storage buffer. Because of the fragility of the crystals, this cryosolution was added directly to the crystallization drop in two successive additions of 1 μL and removal of 1 μL from the opposite side of the drop, followed by a final addition of 2 μL. The drop was allowed to equilibrate for 2 min after each addition. After the final addition, crystals were looped and flash-frozen in liquid N_2.

Data Collection and Processing. Data were collected at the Advanced Photon Source on Northeastern Collaborative Access Team beamline 24-ID-C on a Pilatus detector, making use of a mini kappa goniometer for the MAD data to ensure simultaneous collection of Bijvoet pairs. HKL2000[30] was used to process all of the data sets. For the MAD data sets, blind boxes were used to block off the top and bottom of the frame during integration because diffraction was anisotropic and reflections did not extend to the top and bottom, whereas there were observable reflections extending to the sides. This integration strategy helped to counter the effects of anisotropy, though it reduced the overall completeness of the data set. The native data set was integrated to 2.27 Å resolution, followed by anisotropic correction using Phaser.[31,32] Data processing statistics are listed in Table S1 of the Supporting Information.

Structure Determination. The structure was determined by MAD phasing. Six iron cluster sites per OOR dimer were found and refined using autoSHARP,[33] with a figure of merit to 3.51 Å resolution of 0.30. The overall phasing power was 0.87. The completeness of the peak data set was 77.6%, with the anomalous data good to 5.90 Å resolution, where the phasing power drops below 1.0. Initial electron density maps were obtained after solvent flattening to 4.50 Å resolution in SHARP.[34]

A polyalanine model with [4Fe-4S] clusters (generated with CHAINSAW[32,35]), based on *D. africanus* PFOR [Protein Data Bank (PDB) entry 2C42; a 1.78 Å resolution structure], was placed in the initial electron density maps using COOT.[36] Any parts of this initial model for which there was no electron density were deleted. Of the six total protein chains in the asymmetric unit, chains A−C correspond to one $\alpha\gamma\beta$ unit and chains D−F correspond to the second $\alpha\gamma\beta$ unit. This initial model was used as a mask for iterative rounds of density modification in DM[32,37] (solvent flattening, histogram matching, 2-fold NCS averaging; the 2-fold noncrystallographic symmetry axis was initially determined with PROFESSS[32]). After a few rounds of building a polyalanine model, phase combination and extension using the partial model and experimental phases to 3.51 Å resolution was performed using SFALL,[32,38] SIGMAA,[32,39] and DM. Side chains were added, and model building was continued at 3.51 Å resolution with iterative rounds of phase combination and density modification, until there was negligible improvement in electron density.

Once 88% of the backbone and 46% of side chains had been built, the partial model was used as a search model for molecular replacement in the native data set. Molecular replacement was performed in Phenix (Phaser-MR)[40] using

DOI: 10.1021/acs.biochem.5b00521
Biochemistry 2015, 54, 4112−4120

data to 4.00 Å resolution. Phases were quickly extended, first to 3.00 Å resolution and finally to 2.27 Å resolution, allowing the model to be built to completion through iterative rounds of refinement (simulated annealing and real-space refinement) using Phenix. NCS restraints were used in early rounds of refinement but were removed once most of the side chains had been added to the model. Geometry restraints for the iron−sulfur clusters were based on *M. thermoacetica* carbon monoxide dehydrogenase/acetyl-CoA synthase (PDB entry 3I01),[41] whereas TPP−ligand restraints were based on the crystal structure of a pyruvate decarboxylase (PDB entry 2VK8).[42] Distances from cysteine ligands to iron−sulfur clusters were moderately restrained with a standard deviation of 0.05 Å, whereas angles were allowed to refine freely. The oxidation state of the clusters in our crystals is not known. Distances and angles of atoms coordinating magnesium were not restrained. Simulated annealing composite-omit maps (made with Phenix Autobuild) were used to validate the final model. The model was built to 98.8% completeness, with the residues in the following chains not having sufficient density to model: A(1), B(1, 2, 215−219), C(313, 314), D(1, 2), E(1, 217−227), and F(313, 314). Solvent water molecules were placed automatically by Phenix using a σ cutoff of 3.5. Prior to refinement, 5.0% of unique reflections from the native data set were set aside as a test data set, from which R_{free} values were calculated. Final refinement statistics are listed in Table S1 of the Supporting Information.

Accessible surface calculations were performed using Mark Gerstein's program,[43] with a surface probe size of 1.4 Å, as implemented at the National Institutes of Health.[44]

RESULTS

The structure of *M. thermoacetica* OOR (Figure 2a) was determined to 2.27 Å resolution (Figure 2a) in two stages. First, a low-resolution structure was determined by MAD methods, and then this low-resolution structure was used for molecular replacement in a high-resolution data set with a different unit cell (see Materials and Methods and Table S1 of the Supporting Information). The resulting asymmetric unit of the high-resolution structure contains one OOR molecule, which is a dimer of trimers, $(\alpha\gamma\beta)_2$,[19] with each $\alpha\gamma\beta$ unit forming a catalytic unit. This oligomeric state is in contrast to *Da* PFOR, which is a homodimer, α_2,[14] with the catalytic unit composed of a single polypeptide chain. An alignment of the OOR-α, -γ, and -β chains to the PFOR α chain, however, shows that both enzymes conserve the same core domain structure (Figure 2b,c).[14,19] Chain OOR-α contains domains I and II, chain OOR-γ domains III and V, and chain OOR-β domain VI. Notable differences present in the domain architecture of OOR include the lack of domains IV and VII. The linker that connects domains III and V in OOR (residues 218−237 of OOR-γ) contains no tertiary structure and is thus not a domain, and the C-terminus of OOR-β occurs before the corresponding start of domain VII in *Da* PFOR. Also missing is a four-helix bundle insertion in domain VI of *Da* PFOR that has unknown function. Even with these differences, the resemblance between the OOR $(\alpha\gamma\beta)_2$ dimer and the PFOR α_2 dimer is striking (see Figure S2 of the Supporting Information).

The roles of the domains of OOR, when known, also appear to correspond to those of the domains in PFOR. Domain I constitutes half of the TPP-binding region, providing the residues that interact with the pyrimidine moiety of thiamine. Domain II is the so-called transketolase C-terminal (TKC) domain that, apart from being common to the OFOR and transketolase families of enzymes, has no known function.[45] Domain III, unique to the OFORs, likewise has an undetermined function. Domain V is the ferredoxin domain, coordinating and positioning the medial ($[4Fe\text{-}4S]_{med}$) and distal ($[4Fe\text{-}4S]_{dist}$) iron−sulfur clusters in the electron transport chain. Domain VI is the second half of the TPP-binding region, coordinating magnesium and the pyrophosphate moiety of TPP. Unique among TPP-utilizing enzymes, domain VI in the OFORs also coordinates an iron−sulfur cluster ($[4Fe\text{-}4S]_{prox}$), which is proximal to the active site.

The Electron-Transfer Chain Is Conserved between OOR and PFOR. The arrangement of redox cofactors in *Da* PFOR is almost perfectly conserved in OOR (Figure 3a). Even

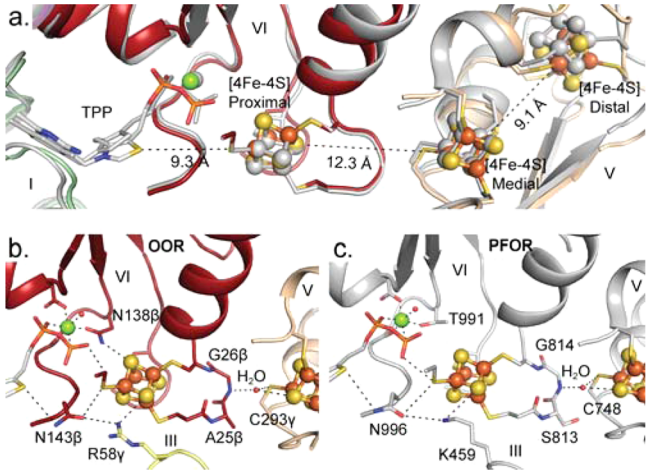

Figure 3. Electron-transfer pathway. (a) An overlay of the electron-transfer pathways of OOR and *Da* PFOR (PDB entry 2C42) shows spatial conservation of the redox cofactors. The structures are aligned by domains I and VI. OOR is colored as in Figure 2, whereas PFOR is colored gray. [4Fe-4S] clusters are shown in ball-and-stick representation, and TPP is shown as sticks and Mg^{2+} as a green sphere. Domains and cofactors are labeled, as are nearest-atom distances between the redox-active portions of the cofactors. (b) View of the electron-transfer pathway in OOR between TPP and the medial [4Fe-4S] cluster. Notable interactions, with interatomic distances of ~4 Å or less, are indicated by dashed lines. (c) View of the electron-transfer pathway in PFOR parallel to that of OOR shown in panel b.

though domain V is found on a chain separate from that of domains I and VI, there is minimal deviation in the positions of the medial and distal clusters, and the distances for electron transfer differ by no more than 0.4 Å. Additionally, conserved protein features around the electron-transfer pathway may provide clues about which features are important for tuning the redox properties of the clusters, as well as facilitating electron transfer (Figure 3b,c). In both OOR and PFOR, the pyrophosphate moiety of TPP is <4 Å from Sγ of Cys52β (Cys840 in PFOR), which ligates the proximal cluster. Both enzymes also have Asn143β (Asn996 in PFOR), which is positioned halfway between the thiazole ring of TPP and the proximal cluster. Also of note is a conserved positively charged residue, Arg58γ in OOR and Lys459 in PFOR, that lies within hydrogen bonding distance of the proximal cluster. Finally, in both OOR and PFOR, the proximal cluster is ligated by a CXGC (residues 24−27 of OOR-β) motif that also interacts directly with the ferredoxin domain. This motif is further emphasized by a water molecule, found in both PFOR and

DOI: 10.1021/acs.biochem.5b00521
Biochemistry 2015, 54, 4112−4120

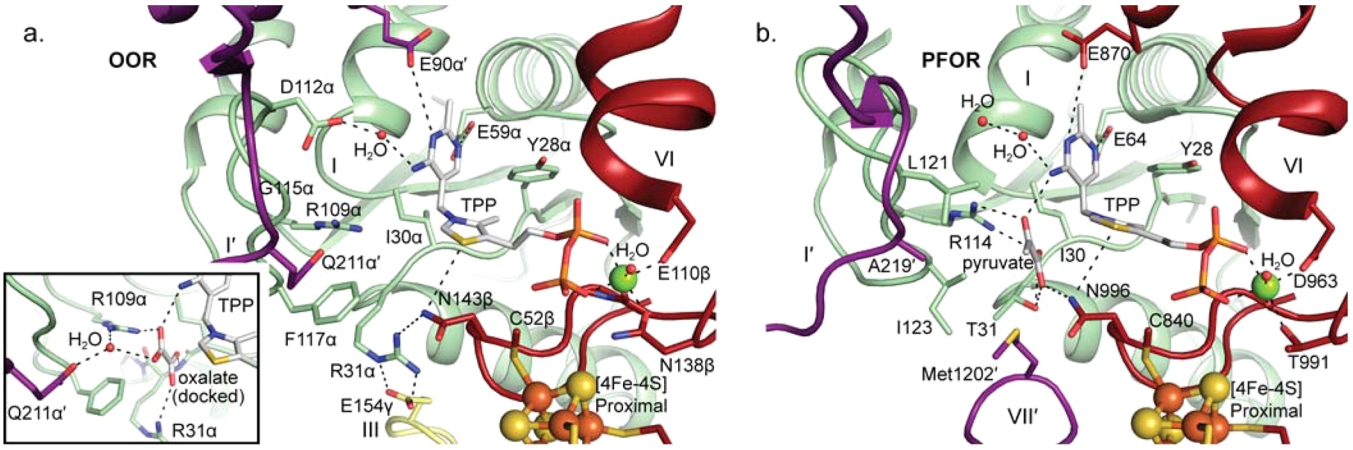

Figure 4. Active sites of OOR and *Da* PFOR. (a) The active site of OOR is shown with TPP in the middle and the substrate-binding pocket directly to the left, bounded by Arg109α, Gln211α', Phe117α, Arg31α, and Asn143β. Some solvent molecules have been omitted for the sake of clarity. Domains are labeled and colored as in Figure 2. Cofactors and select residue side chains are labeled and shown as sticks. Coordination to Mg^{2+} (green sphere) and other important short interatomic distances (less than ~4 Å) are shown with dashed lines. The inset shows a docking model for oxalate binding based on pyruvate binding in PFOR. Short interatomic distances to the docked oxalate are shown with dashed lines. A water molecule omitted in the main figure is shown here interacting with Arg109α, Gln211α', and the docked oxalate molecule. (b) The active site of PFOR (PDB entry 2C42) has TPP, the proximal [4Fe-4S] cluster, and bound pyruvate shown as sticks. Domains are labeled and colored as follows: I, green; VI, red; I′ and VII′, purple. Coordination to Mg^{2+} (green sphere) and other important short interatomic distances (less than ~4 Å) are indicated with dashed lines.

OOR structures, positioned within hydrogen bonding distance of the glycine backbone nitrogen, and one of the sulfur atoms in the medial cluster (Figure 3b,c).

One obvious difference in the electron-transfer pathways between OOR and PFOR is the relative size of the ferredoxin domains (see Figure S3 of the Supporting Information). A minimal ferredoxin fold with 33% sequence identity is found in domain V of both enzymes, along with similar electrostatics around the clusters. PFOR, however, contains a 27-residue insertion that makes its domain V 50% larger than that in OOR. This insertion does not coordinate the clusters and is primarily solvent-exposed, and its absence appears to only minimally affect access of the solvent to the clusters (the distal cluster is 0 and 2.5% solvent accessible in PFOR and OOR, respectively).

Similar Active Site Structures Provide Clues about Enzyme Specificity. At first glance, the active sites of OOR and PFOR look remarkably similar (Figure 4). The TPP-binding motif appears to be functionally conserved, including the strictly conserved Glu59α (Glu64 in PFOR), as well as a $GDGX_{29}YXN$ (residues 109−143 of OOR-β) helix−helix−strand Mg^{2+}-pyrophosphate-binding motif that is typically found in TPP-utilizing enzymes. Both enzymes also have a glutamate residue making a potential hydrogen bond with N3′ of the TPP pyrimidine ring, though this residue comes from different domains in each enzyme: Glu90α' from domain I of the opposite monomeric unit in OOR and Glu870 from domain VI in PFOR (Figure 4; also see Figure S4 of the Supporting Information). [A prime following a residue or domain name (as in Glu90α' or domain VII′) indicates that the residue or domain is from the opposite monomeric unit.] Finally, in OOR, Asp112α from domain I interacts indirectly through a water molecule with the imino group of the TPP pyrimidine and may have a role in preparing TPP for catalysis, though there is no analogous interaction in *Da* PFOR.[14]

The similarities between OOR and PFOR also extend to the substrate-binding pocket. For PFOR, a structure is available depicting substrate (pyruvate)−protein interactions at 1.78 Å resolution (Figure 4b). This structure was captured through a crystal soaking experiment at low pH (6.0) where the activity of PFOR is substantially diminished.[16] Using the position of pyruvate as a guide, we can compare the active sites of OOR and PFOR (Figure 4). We find that both enzymes have Arg109α (Arg114 in PFOR) directed toward the active site; this arginine can form hydrogen bonds with pyruvate in PFOR and provide a balancing positive charge to the negatively charged pyruvate, a functionality that could carry over to oxalate binding in OOR. Asn143β, mentioned above with respect to the electron-transfer pathway, is also positioned to interact with substrate in the active site.

One substantial difference in the substrate-binding pocket was predicted by sequence alignments.[19] A YPITP active site motif that is conserved in PFORs (residues 28−32 in *Da* PFOR) is altered to a YPIRP motif in OOR (residues 28−32 of OOR-α). In this motif, Tyr and Ile help to prop up TPP in the so-called "V conformation" that facilitates catalysis (Figure 4).[46] In PFOR, Thr of the YPITP motif provides hydrogen bonding interactions to bound pyruvate. The substitution of Thr with Arg in OOR was hypothesized to provide an extra positively charged residue in the substrate-binding pocket, to facilitate binding of the additionally negatively charged oxalate molecule.[19] The structure of OOR reveals that indeed, Arg31α is positioned to do just that. Arg31α also substitutes for Met1202′ of *Da* PFOR in providing a floor to the substrate-binding pocket (Figure 4). Interestingly, Met1202′ is from domain VII′ of *Da* PFOR and is not present in other PFORs or OFORs. In *Da* PFOR, this domain extends from one monomer to wrap around and insert into the active site of the other monomer (see Figure S5 of the Supporting Information). OOR fills part of this void with Arg31α (Figure 4).

Three other active site substitutions in OOR are (PFOR → OOR) Leu121 → Gly115α, Ile123 → Phe117α, and Ala219′ → Gln211α'. The first two substitutions remove large aliphatic side chains from the active site, which in PFOR serve to provide hydrophobic interactions with the methyl group of pyruvate. Opening the OOR active site in this way makes room for the third substituted residue, Gln211α' from domain I of the

DOI: 10.1021/acs.biochem.5b00521
Biochemistry 2015, 54, 4112−4120

opposite monomeric unit, to provide for hydrophilic interactions in the substrate-binding pocket. Taken together, these active site substitutions in OOR make the substrate-binding pocket substantially more hydrophilic and potentially more amenable to oxalate binding than the active site of PFOR.

The Lack of a Domain VII Does Not Necessarily Create a More Accessible Active Site. In all structures of the *Da* PFOR enzyme, access to the active site is blocked by domain VII of the adjacent monomer (see Figure S5 of the Supporting Information), raising the question of how a large substrate like CoA is able to reach the TPP cofactor. OOR does not have domain VII, and we were expecting to find a more open active site as a result. However, we find that a 13-residue insert into domain III, one of the few large inserts in OOR relative to PFOR, transforms what is a small turn in PFOR into an extended loop that occupies the same cavity in OOR as domain VII in PFOR (Figure 5). In addition to restricting access of solvent to the active site, this domain III loop has a glutamate residue (Glu154γ) that forms a salt bridge to Arg31α (the residue that replaces PFOR's Met1202′ from domain VII′). Thus, contrary to our expectations, access of solvent to TPP is not as different in OOR from that in PFOR.

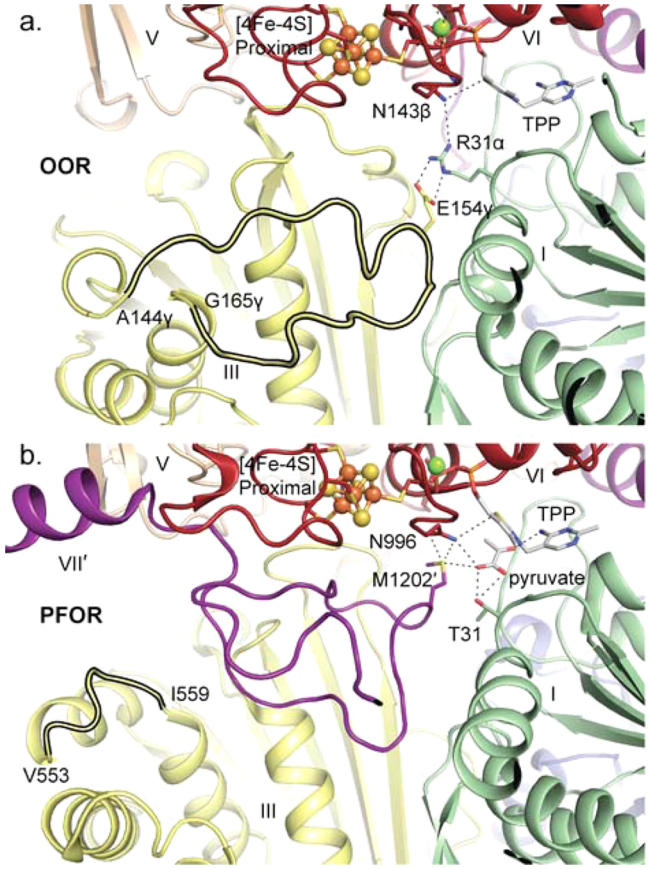

Figure 5. Channels to the active sites of OOR and *Da* PFOR are plugged by different structural features. (a) The channel to the OOR active site, running among domains III, I, and VI, is occupied by an unstructured loop inserted into domain III between Ala144γ and Gly165γ. Glu154γ makes a salt bridge to Arg31α, which in turn interacts with the substrate-binding pocket. Notable short interatomic distances (less than ~ 4 Å) are indicated by dashed lines. (b) Access to the active site in *Da* PFOR is shown in the same orientation as in panel a, with the same coloring scheme for domains I–VI. Domain VII′, which occupies this channel in the structure of PFOR, is colored purple. In this structure, Met1202′ interacts with the pyruvate-binding site, providing a floor to the active site. These close contacts to Met1202′ are indicated by dashed lines, which also indicate short distances, as in panel a.

DISCUSSION

OOR is only the second enzyme of the superfamily of 2-oxoacid:ferredoxin oxidoreductases to be structurally characterized. The similarities between OOR and *Da* PFOR are reflected in the domain architecture, which is conserved within OFORs. Apart from the requirement for TPP, the similarities between these enzymes are best understood from the perspective of the low-potential electrons in the substrate carbon–carbon bond.

In PFOR, pyruvate is first decarboxylated to form a TPP-hydroxyethyl [HE-TPP] species, which then undergoes two one-electron oxidations involving a chain of three [4Fe-4S] clusters.[47,48] The crystal structure of *Da* PFOR revealed the spatial arrangement of the three [4Fe-4S] clusters, which are coordinated by domains V and VI.[14] The distances between all the redox cofactors (TPP to $[4Fe\text{-}4S]_{prox}$ to $[4Fe\text{-}4S]_{med}$ to $[4Fe\text{-}4S]_{dist}$) are all within the range for electron transfer between protein-bound redox cofactors. In addition, the medial and distal clusters are positioned close to the surface of the protein, where they can transfer electrons to other electron-transfer proteins or directly to other redox enzymes.

Here we find that the three [4Fe-4S] clusters of OOR are positioned almost identically despite substantial deletions in domains V and VI of OOR relative to *Da* PFOR. Domain V especially, though 50% larger in PFOR than in OOR, maintains a core ferredoxin fold and cluster environment in both enzymes. Interestingly, OFORs have a wide variety of insertions and deletions in their ferredoxin domains, with hundreds of enzymes that have minimal ferredoxin domains like that of OOR. Because these variably sized insertions do not disrupt the "core" fold, it is likely that these modifications may have evolved to affect intermolecular protein–protein interactions within the cell, such as would be required between the OFOR and its cognate redox partner protein. More work, however, must be done to ascertain the reduction potentials of the OOR clusters to understand better how these domains function.

In addition to the position of the redox cofactors and environment of the ferredoxin clusters, the proximal cluster maintains what appear to be key interactions with nearby residues. Asn143β of domain VI interacts with both TPP and the proximal cluster and is poised to interact with substrate as well. This interaction would place any TPP-bound intermediates within the tertiary coordination sphere of the proximal cluster and may have a role in facilitating electron transfer during catalysis. Arg58γ of domain III is functionally conserved in PFOR as Lys459, so that both enzymes have a positively charged residue interacting with both Asn143β and the proximal cluster. This similarity between OOR and PFOR structures suggests a possible role for domain III, whose function has been enigmatic, in modulating the reduction potential of the proximal cluster. Finally, the CAGC motif that provides two cysteine ligands to the proximal cluster in OOR is conserved as a CXGC motif in all OFORs (see Figure S6 of the Supporting Information). Both PFOR and OOR structures show identical positioning of motif residues in the gap between the proximal cluster and the medial cluster, complete with a conserved water molecule that sits between the motif and the medial cluster (Figure 3b,c). This water is in position to form

DOI: 10.1021/acs.biochem.5b00521
Biochemistry 2015, 54, 4112–4120

hydrogen bonds to both the glycine backbone nitrogen of the motif and a sulfur of the medial cluster. Thus, CXGC residues contact the proximal cluster directly using the two cysteine residues and contact the medial cluster indirectly through this conserved water molecule. Further work will be required to determine if this conserved water plays a role in mediating electron transfer between these two clusters.

OOR and PFOR operate on very different substrates. Pyruvate is a typical 2-oxoacid, consisting of one negatively charged acid group, one electrophilic carbonyl, and a hydrophobic methyl group. Oxalate, on the other hand, is a dicarboxylic acid, containing two hydrophilic negatively charged acidic groups,[49] neither of which is particularly electrophilic. From the perspective of TPP, pyruvate is a much better target for nucleophilic attack than oxalate. The difficulty of activating oxalate for catalysis is seen in the anaerobic oxalyl-CoA decarboxylase pathway, which first makes use of formyl-CoA transferase to activate oxalate to form oxalyl-CoA. The thioester in oxalyl-CoA is more electrophilic than a carboxylate group, making it a better target for nucleophilic attack by TPP. In aerobic pathways, Mn^{2+} presumably allows the generation of a radical species that results in cleavage of the carbon−carbon bond of oxalate, though the mechanistic details are still murky.[50] *M. thermoacetica*, on the other hand, is capable of activating oxalate for nucleophilic attack without the aid of CoA, a feat that can now be better understood by comparing the active sites of OOR and PFOR.

The active site of PFOR is tailored for pyruvate binding.[14] The carboxylate of pyruvate interacts with various hydrogen bond donors, including a protein backbone amide (Ile30-Thr31), Thr31, Asn996, and Arg114, which also provides an ionic interaction. The carbonyl group of pyruvate interacts with the imine from TPP as well as Arg114 (Figure 4b). With Arg114 providing two hydrogen bonds, a total of six hydrogen bond donor interactions and one positive charge are provided by the active site to bind pyruvate. The methyl group is not neglected; PFOR provides Leu121 and Ile123 for hydrophobic interactions with pyruvate.

OOR's active site has a number of substitutions relative to PFOR that make it amenable to binding oxalate. In domain I, Thr31 has been substituted with an arginine, and the structure shows that Arg31α is positioned for interacting with the substrate. Leu121 and Ile123 in PFOR are substituted with Gly115α and Phe117α in OOR, respectively, allowing access to the active site for an interaction with Gln211α'. Together with TPP and Asn143β, the OOR active site provides seven hydrogen bond donors all pointing toward the presumed substrate-binding site, including two cationic interactions, to stabilize the binding of oxalate. Thus, the substrate-binding pocket in OOR is more positively charged and hydrophilic than that in PFOR. Beyond substrate binding, these hydrogen bond donors may also stabilize resonance structures of oxalate that are more electrophilic in nature, potentially making it a more favorable target for nucleophilic attack by TPP.

The question of access to the active site is important for PFORs and other OFORs in general because of the requirement for CoA to complete the catalytic cycle. Although multiple structures of *Da* PFOR have been obtained, a structure in complex with CoA remains to be determined. It is possible that the C-terminal domain VII that is peculiar to the *Da* enzyme, and which occupies a central cavity that leads directly to the active site, is blocking the CoA-binding site in the crystal. However, without further evidence, the question of CoA binding to PFOR remains open.

OOR, like other OFORs, does not have a domain VII, so it was hypothesized that the OOR structure might reveal how substrates of OFORs access the active site. It was a surprise, therefore, when an extended loop from domain III of OOR (residues 144−165 of OOR-γ) was observed to fill the cavity left empty by the lack of a domain VII, completely blocking access to the active site. This loop links two helices in the C-terminal end of domain III and is 13 residues longer than the corresponding linker in *Da* PFOR. Apart from Glu154γ, which forms a salt bridge to Arg31α in the active site, this loop makes no substantial interactions with the surrounding protein. This extended loop is conserved only in enzymes that are >65% identical to *M. thermacetica* OOR, so it does not appear that this loop will be a hallmark of OORs. It does, however, show how predictions of substrate channels or solvent accessibility are challenging in this family of enzymes, with the potential for simple insertions at loop positions to substantially alter the active site environment.

CONCLUSION

Structures of OOR and PFOR show similarities where we expected differences and differences where we expected similarities. Despite the fact that the catalytic unit of *Da* PFOR consists of one peptide chain with seven domains, the trimeric structure of the OOR catalytic unit with five domains is quite similar in overall architecture. We see how a trimmed ferredoxin domain can house an almost identical arrangement of iron−sulfur clusters and how a loop can replace domain VII to seal a channel to the active site. These structural data also show how substitutions in an OFOR active site can allow for activation of a relatively nonreactive substrate, in this case oxalate. Overall, the structural similarities and differences between OOR and PFOR provide a framework for understanding how nature harvests the low-potential electrons that are essential for fundamental processes such as nitrogen and carbon fixation, and they serve to inform about the larger family of OFOR enzymes that are pervasive throughout microbial life.

ASSOCIATED CONTENT

Supporting Information

Crystallographic data collection and refinement statistics (Table S1) and additional figures (Figures S1−S6). Accession Codes: The atomic coordinates have been deposited in the Protein Data Bank as entry 5C4I. The Supporting Information is available free of charge on the ACS Publications website at DOI: 10.1021/acs.biochem.5b00521.

AUTHOR INFORMATION

Corresponding Author

*E-mail: cdrennan@mit.edu. Telephone: (617) 253-5622.

Present Address

⊥E.P.: Department of Medicinal Chemistry, University of Utah, Salt Lake City, UT 84112.

Funding

This work was supported in part by National Institutes of Health Grants GM069857 (C.L.D.) and GM39451 (S.W.R.) and by the National Science Foundation (NSF) Graduate Research Fellowship under Grant 1122374 (M.I.G.). This research was also made possible by the support of the Martin

DOI: 10.1021/acs.biochem.5b00521
Biochemistry 2015, 54, 4112−4120

Family Society of Fellows for Sustainability (M.I.G.). C.L.D. is a Howard Hughes Medical Institute Investigator.

Notes

The authors declare no competing financial interest.

■ ACKNOWLEDGMENTS

This work is based upon research conducted at the Advanced Photon Source on the Northeastern Collaborative Access Team beamlines, which are supported by a grant from the National Institute of General Medical Sciences (P41 GM103403) and the National Institutes of Health. This research used resources of the Advanced Photon Source, a U.S. Department of Energy (DOE) Office of Science User Facility operated for the DOE Office of Science by Argonne National Laboratory under Contract DE-AC02-06CH11357.

■ ABBREVIATIONS

TPP, thiamine pyrophosphate; OFOR, 2-oxoacid:ferredoxin oxidoreductase; OOR, oxalate oxidoreductase; PFOR, pyruvate:ferredoxin oxidoreductase; CoA, coenzyme A; W–L, Wood–Ljungdahl; *Mt*, *M. thermoacetica*; *Da*, *D. africanus*; MAD, multiwavelength anomalous dispersion; [HE-TPP], hydroxyethyl-TPP.

■ REFERENCES

(1) Kletzin, A., and Adams, M. W. (1996) Molecular and Phylogenetic Characterization of Pyruvate and 2-Ketoisovalerate Ferredoxin Oxidoreductases from *Pyrococcus furiosus* and Pyruvate Ferredoxin Oxidoreductase from *Thermotoga maritima*. *J. Bacteriol. 178* (1), 248–257.

(2) Horner, D. S., Hirt, R. P., and Embley, T. M. (1999) A Single Eubacterial Origin of Eukaryotic Pyruvate: Ferredoxin Oxidoreductase Genes: Implications for the Evolution of Anaerobic Eukaryotes. *Mol. Biol. Evol. 16* (9), 1280–1291.

(3) Fuchs, G. (2011) Alternative Pathways of Carbon Dioxide Fixation: Insights into the Early Evolution of Life? *Annu. Rev. Microbiol. 65* (1), 631–658.

(4) Quandt, L., Pfennig, N., and Gottschalk, G. (1978) Evidence for the Key Position of Pyruvate Synthase in the Assimilation of CO_2 by *Chlorobium*. *FEMS Microbiol. Lett. 3* (4), 227–230.

(5) Fuchs, G., Stupperich, E., and Eden, G. (1980) Autotrophic CO_2 Fixation in *Chlorobium limicola*. Evidence for the Operation of a Reductive Tricarboxylic Acid Cycle in Growing Cells. *Arch. Microbiol. 128* (1), 64–71.

(6) Furdui, C., and Ragsdale, S. W. (2000) The Role of Pyruvate Ferredoxin Oxidoreductase in Pyruvate Synthesis during Autotrophic Growth by the Wood-Ljungdahl Pathway. *J. Biol. Chem. 275* (37), 28494–28499.

(7) Noor, E., Bar-Even, A., Flamholz, A., Lubling, Y., Davidi, D., and Milo, R. (2012) An Integrated Open Framework for Thermodynamics of Reactions That Combines Accuracy and Coverage. *Bioinformatics 28* (15), 2037–2044.

(8) Noor, E., Haraldsdóttir, H. S., Milo, R., and Fleming, R. M. T. (2013) Consistent Estimation of Gibbs Energy Using Component Contributions. *PLoS Comput. Biol. 9* (7), e1003098.

(9) Wahl, R. C., and Orme-Johnson, W. H. (1987) Clostridial Pyruvate Oxidoreductase and the Pyruvate-Oxidizing Enzyme Specific to Nitrogen Fixation in *Klebsiella pneumoniae* Are Similar Enzymes. *J. Biol. Chem. 262* (22), 10489–10496.

(10) Yates, M. G. (1967) Stimulation of the Phosphoroclastic System of *Desulfovibrio* by Nucleotide Triphosphates. *Biochem. J. 103*, 32c–34c.

(11) Peck, H. D., Jr. (1993) Bioenergetic Strategies of the Sulfate-Reducing Bacteria. In *The Sulfate-Reducing Bacteria: Contemporary Perspectives* (Odom, J. M., and Singleton, R. J., Eds.) pp 41–76, Brock/Springer Series in Contemporary Bioscience, Springer, New York.

(12) Dörner, E., and Boll, M. (2002) Properties of 2-Oxoglutarate:Ferredoxin Oxidoreductase from *Thauera aromatica* and Its Role in Enzymatic Reduction of the Aromatic Ring. *J. Bacteriol. 184* (14), 3975–3983.

(13) Yarlett, N., Gorrell, T. E., Marczak, R., and Müller, M. (1985) Reduction of Nitroimidazole Derivatives by Hydrogenosomal Extracts of *Trichomonas vaginalis*. *Mol. Biochem. Parasitol. 14* (1), 29–40.

(14) Chabrière, E., Charon, M.-H., Volbeda, A., Pieulle, L., Hatchikian, E. C., and Fontecilla-Camps, J.-C. (1999) Crystal Structures of the Key Anaerobic Enzyme Pyruvate:ferredoxin Oxidoreductase, Free and in Complex with Pyruvate. *Nat. Struct. Mol. Biol. 6* (2), 182–190.

(15) Chabrière, E., Vernède, X., Guigliarelli, B., Charon, M.-H., Hatchikian, E. C., and Fontecilla-Camps, J. C. (2001) Crystal Structure of the Free Radical Intermediate of Pyruvate:Ferredoxin Oxidoreductase. *Science 294* (5551), 2559–2563.

(16) Cavazza, C., Contreras-Martel, C., Pieulle, L., Chabrière, E., Hatchikian, E. C., and Fontecilla-Camps, J. C. (2006) Flexibility of Thiamine Diphosphate Revealed by Kinetic Crystallographic Studies of the Reaction of Pyruvate-Ferredoxin Oxidoreductase with Pyruvate. *Structure 14* (2), 217–224.

(17) Daniel, S. L., and Drake, H. L. (1993) Oxalate- and Glyoxylate-Dependent Growth and Acetogenesis by *Clostridium thermoaceticum*. *Appl. Environ. Microbiol. 59* (9), 3062–3069.

(18) Daniel, S. L., Pilsl, C., and Drake, H. L. (2004) Oxalate Metabolism by the Acetogenic Bacterium *Moorella thermoacetica*. *FEMS Microbiol. Lett. 231* (1), 39–43.

(19) Pierce, E., Becker, D. F., and Ragsdale, S. W. (2010) Identification and Characterization of Oxalate Oxidoreductase, a Novel Thiamine Pyrophosphate-Dependent 2-Oxoacid Oxidoreductase That Enables Anaerobic Growth on Oxalate. *J. Biol. Chem. 285* (52), 40515–40524.

(20) Kotsira, V. P., and Clonis, Y. D. (1997) Oxalate Oxidase from Barley Roots: Purification to Homogeneity and Study of Some Molecular, Catalytic, and Binding Properties. *Arch. Biochem. Biophys. 340* (2), 239–249.

(21) Zhou, F., Zhang, Z., Gregersen, P. L., Mikkelson, J. D., de Neergaard, E., Collinge, D. B., and Thordal-Christensen, H. (1998) Molecular Characterization of the Oxalate Oxidase Involved in the Response of Barley to the Powdery Mildew Fungus. *Plant Physiol. 117* (1), 33–41.

(22) Whittaker, M. M., and Whittaker, J. W. (2002) Characterization of Recombinant Barley Oxalate Oxidase Expressed by *Pichia pastoris*. *JBIC, J. Biol. Inorg. Chem. 7* (1–2), 136–145.

(23) Tanner, A., and Bornemann, S. (2000) *Bacillus subtilis* YvrK Is an Acid-Induced Oxalate Decarboxylase. *J. Bacteriol. 182* (18), 5271–5273.

(24) Jakoby, W. B., Ohmura, E., and Hayaishi, O. (1956) Enzymatic Decarboxylation of Oxalic Acid. *J. Biol. Chem. 222* (1), 435–446.

(25) Quayle, J. R. (1963) Carbon Assimilation by *Pseudomonas oxalaticus* (Ox 1). 7. Decarboxylation of Oxalyl-Coenzyme A to Formyl-Coenzyme A. *Biochem. J. 89*, 492–503.

(26) Anantharam, V., Allison, M. J., and Maloney, P. C. (1989) Oxalate:formate Exchange. The Basis for Energy Coupling in *Oxalobacter*. *J. Biol. Chem. 264* (13), 7244–7250.

(27) Hodgkinson, A. (1977) *Oxalic Acid in Biology and Medicine*, Academic Press, London.

(28) Seifritz, C., Fröstl, J. M., Drake, H. L., and Daniel, S. L. (2002) Influence of Nitrate on Oxalate- and Glyoxylate-Dependent Growth and Acetogenesis by *Moorella thermoacetica*. *Arch. Microbiol. 178* (6), 457–464.

(29) Elliott, J. I., and Brewer, J. M. (1978) The Inactivation of Yeast Enolase by 2,3-Butanedione. *Arch. Biochem. Biophys. 190* (1), 351–357.

(30) Otwinowski, Z., and Minor, W. (1997) Processing of X-ray Diffraction Data Collected in Oscillation Mode. In *Macromolecular Crystallography, part A* (Carter, C. W., Jr., and Sweet, R. M., Eds.) Vol. *276*, pp 307–326, Methods in Enzymology, Academic Press, New York.

DOI: 10.1021/acs.biochem.5b00521
Biochemistry 2015, 54, 4112–4120

(31) McCoy, A. J., Grosse-Kunstleve, R. W., Adams, P. D., Winn, M. D., Storoni, L. C., and Read, R. J. (2007) *Phaser* Crystallographic Software. *J. Appl. Crystallogr. 40* (4), 658−674.
(32) Winn, M. D., Ballard, C. C., Cowtan, K. D., Dodson, E. J., Emsley, P., Evans, P. R., Keegan, R. M., Krissinel, E. B., Leslie, A. G. W., McCoy, A., McNicholas, S. J., Murshudov, G. N., Pannu, N. S., Potterton, E. A., Powell, H. R., Read, R. J., Vagin, A., and Wilson, K. S. (2011) Overview of the CCP4 Suite and Current Developments. *Acta Crystallogr. D67* (Part 4), 235−242.
(33) Vonrhein, C., Blanc, E., Roversi, P., and Bricogne, G. (2007) Automated Structure Solution with autoSHARP. In *Macromolecular Crystallography Protocols* (Doublié, S., Ed.) pp 215−230, Methods in Molecular Biology, Humana Press, Totowa, NJ.
(34) Bricogne, G., Vonrhein, C., Flensburg, C., Schiltz, M., and Paciorek, W. (2003) Generation, Representation and Flow of Phase Information in Structure Determination: Recent Developments in and around *SHARP* 2.0. *Acta Crystallogr. D59* (11), 2023−2030.
(35) Stein, N. (2008) *CHAINSAW*: A Program for Mutating Pdb Files Used as Templates in Molecular Replacement. *J. Appl. Crystallogr. 41* (3), 641−643.
(36) Emsley, P., Lohkamp, B., Scott, W. G., and Cowtan, K. (2010) Features and Development of *Coot*. *Acta Crystallogr. D66* (4), 486−501.
(37) Cowtan, K. D. (1994) "DM": An Automated Procedure for Phase Improvement by Density Modification. *Joint CCP4 ESF-EACBM Newsletter of Protein Crystallography 31*, 34−38.
(38) Agarwal, R. C. (1978) A New Least-Squares Refinement Technique Based on the Fast Fourier Transform Algorithm. *Acta Crystallogr. A34* (5), 791−809.
(39) Read, R. J. (1986) Improved Fourier Coefficients for Maps Using Phases from Partial Structures with Errors. *Acta Crystallogr. A42* (3), 140−149.
(40) Adams, P. D., Afonine, P. V., Bunkóczi, G., Chen, V. B., Davis, I. W., Echols, N., Headd, J. J., Hung, L.-W., Kapral, G. J., Grosse-Kunstleve, R. W., McCoy, A. J., Moriarty, N. W., Oeffner, R., Read, R. J., Richardson, D. C., Richardson, J. S., Terwilliger, T. C., and Zwart, P. H. (2010) *PHENIX*: A Comprehensive Python-Based System for Macromolecular Structure Solution. *Acta Crystallogr. D66* (2), 213−221.
(41) Kung, Y., Doukov, T. I., Seravalli, J., Ragsdale, S. W., and Drennan, C. L. (2009) Crystallographic Snapshots of Cyanide- and Water-Bound C-Clusters from Bifunctional Carbon Monoxide Dehydrogenase/Acetyl-CoA Synthase. *Biochemistry 48* (31), 7432−7440.
(42) Kutter, S., Weiss, M. S., Wille, G., Golbik, R., Spinka, M., and König, S. (2009) Covalently Bound Substrate at the Regulatory Site of Yeast Pyruvate Decarboxylases Triggers Allosteric Enzyme Activation. *J. Biol. Chem. 284* (18), 12136−12144.
(43) Gerstein, M., and Richards, F. M. (2001) Protein Geometry: Distances, Areas, and Volumes. In *International Tables for Crystallography* (Rossmann, M., and Arnold, E., Eds.) Vol. *F*, pp 531−539, Kluwer, Dordrecht, The Netherlands.
(44) http://helixweb.nih.gov/structbio/.
(45) Costelloe, S. J., Ward, J. M., and Dalby, P. A. (2008) Evolutionary Analysis of the TPP-Dependent Enzyme Family. *J. Mol. Evol. 66* (1), 36−49.
(46) Guo, F., Zhang, D., Kahyaoglu, A., Farid, R. S., and Jordan, F. (1998) Is a Hydrophobic Amino Acid Required to Maintain the Reactive V Conformation of Thiamin at the Active Center of Thiamin Diphosphate-Requiring Enzymes? Experimental and Computational Studies of Isoleucine 415 of Yeast Pyruvate Decarboxylase. *Biochemistry 37* (38), 13379−13391.
(47) Cammack, R., Kerscher, L., and Oesterhelt, D. (1980) A Stable Free Radical Intermediate in the Reaction of 2-Oxoacid:ferredoxin Oxidoreductases of *Halobacterium halobium*. *FEBS Lett. 118* (2), 271−273.
(48) Astashkin, A. V., Seravalli, J., Mansoorabadi, S. O., Reed, G. H., and Ragsdale, S. W. (2006) Pulsed Electron Paramagnetic Resonance Experiments Identify the Paramagnetic Intermediates in the Pyruvate Ferredoxin Oxidoreductase Catalytic Cycle. *J. Am. Chem. Soc. 128* (12), 3888−3889.
(49) Haynes, W. M., Ed. (2015) *CRC Handbook of Chemistry and Physics*, 95th ed., CRC Press/Taylor and Francis, Boca Raton, FL.
(50) Whittaker, M. M., Pan, H.-Y., Yukl, E. T., and Whittaker, J. W. (2007) Burst Kinetics and Redox Transformations of the Active Site Manganese Ion in Oxalate Oxidase. *J. Biol. Chem. 282* (10), 7011−7023.

DOI: 10.1021/acs.biochem.5b00521
Biochemistry 2015, 54, 4112−4120